Kinetic-scale Current Sheets in the Solar Wind at 1 au: Scale-dependent Properties and Critical Current Density

I. Y. Vasko[1,2] , K. Alimov[1], T. Phan[1] , S. D. Bale[1,3] , F. S. Mozer[1] , and A. V. Artemyev[2,4]
[1] Space Sciences Laboratory, University of California at Berkeley, Berkeley, CA 94720, USA; vaskoiy@berkeley.edu
[2] Space Research Institute of Russian Academy of Sciences, Moscow, Russia
[3] Department of Physics, University of California at Berkeley, Berkeley, CA 94720, USA
[4] University of California, Los Angeles, CA 90095, USA

Abstract

We present analysis of 17,043 proton kinetic-scale current sheets (CSs) collected over 124 days of Wind spacecraft measurements in the solar wind at 11 samples s^{-1} magnetic field resolution. The CSs have thickness, λ, from a few tens to one thousand kilometers with typical values around 100 km, or within about $0.1–10\lambda_p$ in terms of local proton inertial length, λ_p. We found that the current density is larger for smaller-scale CSs, $J_0 \approx 6\,\mathrm{nA\,m^{-2}} \cdot (\lambda/100\,\mathrm{km})^{-0.56}$, but does not statistically exceed a critical value, J_A, corresponding to the drift between ions and electrons of local Alvén speed. The observed trend holds in normalized units: $J_0/J_A \approx 0.17 \cdot (\lambda/\lambda_p)^{-0.51}$. The CSs are statistically force-free with magnetic shear angle correlated with CS spatial scale: $\Delta\theta \approx 19° \cdot (\lambda/\lambda_p)^{0.5}$. The observed correlations are consistent with local turbulence being the source of proton kinetic-scale CSs in the solar wind, while the mechanisms limiting the current density remain to be understood.

Unified Astronomy Thesaurus concepts: Interplanetary turbulence (830); Solar wind (1534)

1. Introduction

The understanding of turbulence dissipation and plasma heating in a weakly collisionless plasma is of fundamental importance for numerous astrophysical systems (e.g., Matthaeus & Velli 2011). Numerical simulations have shown that turbulence dissipation should be spatially intermittent with substantial plasma heating localized in and around coherent structures, such as current sheets (CSs), which occupy a relatively small volume (Karimabadi et al. 2013; Zhdankin et al. 2013, 2014; Wan et al. 2014, 2016). Numerical simulations have also shown that magnetic reconnection in kinetic-scale CSs produced by turbulence not only results in plasma heating, but also fundamentally affects development of the turbulence cascade at sub-proton scales (e.g., Servidio et al. 2015; Cerri & Califano 2017; Franci et al. 2017; Papini et al. 2019). Modern simulations are still incapable of entirely reproducing the complex dynamics of realistic three-dimensional plasma turbulence, and substantial effort has been directed toward comparing simulation results with observations in the solar wind, a weakly collisional plasma most accessible for in-situ measurements (e.g., Matteini et al. 2020).

Spacecraft measurements have shown that solar-wind heating should continuously occur within a few tens of solar radii of the Sun, as well as further out in the heliosphere, and dissipation of turbulent magnetic field fluctuations should be the dominant solar-wind heating mechanism (e.g., Kohl et al. 1996; Cranmer et al. 2009; Hellinger et al. 2013). The solar-wind observations revealed turbulence to be dominated by Alfénic fluctuations highly oblique ($k_\perp \gg k_\parallel$) to local mean magnetic field, Kolmogorov-like spectrum $E_{k_\perp} \propto k_\perp^{-5/3}$ at scales larger than proton kinetic scales, and a steeper spectrum $E_{k_\perp} \propto k_\perp^{-2.8}$ at scales smaller than proton kinetic scales (e.g., review by Chen 2016). Numerical

simulations have successfully reproduced these properties of the solar-wind turbulence (e.g., Boldyrev & Perez 2012; Cerri et al. 2017; Franci et al. 2017, 2018; Papini et al. 2019). The crucial unresolved problem is the origin of coherent structures and, specifically, CSs observed in the solar wind, and the very ability of these structures to heat solar wind plasma (e.g., review by Matthaeus et al. 2015). In this Letter we present a statistical analysis of proton kinetic-scale CSs in the solar wind at 1 au, contributing to understanding the origin and dissipation of coherent structures in plasma turbulence.

The presence of CSs on a wide range of temporal scales was established by early spacecraft measurements in the solar wind (Burlaga et al. 1977; Tsurutani & Smith 1979; Lepping & Behannon 1986; Söding et al. 2001). These measurements showed that the magnetic field has more or less constant magnitude, but rotates across a CS through some shear angle. The typical CS thickness was around ten proton inertial lengths, while the occurrence rate at 1 au was a few tens per day. Multispacecraft analysis has shown that the magnetic field component normal to a CS surface is much smaller (if present at all) than local magnetic field magnitude (Horbury et al. 2001; Knetter et al. 2004). The majority of CS studies were limited by magnetic field measurements of relatively low resolution (a few seconds at best) and typically by CSs with shear angles $\gtrsim 30°$ (e.g., Söding et al. 2001; Artemyev et al. 2018, 2019). Devoid of these shortcomings, the analysis by Vasquez et al. (2007) included more than 6000 CSs collected at 1 au using magnetic field measurements at $1/3\,\mathrm{s}$ resolution. The typical thickness of the CSs was around a few proton inertial lengths, and the occurrence rate was about a few hundred CSs per day. Thus, the higher temporal resolution allowed resolving thinner CSs, which turned out to be much more abundant than larger-scale CSs reported in the early studies. Based on the log-normal distribution of waiting times of the CSs, Vasquez et al. (2007) suggested they are produced by local turbulence, in accordance with earlier theoretical hypothesis (e.g., Matthaeus & Lamkin 1986).

This hypothesis was further supported by observations of similar distributions of magnetic field rotations and waiting times of coherent structures in solar-wind and MHD turbulence simulations (Greco et al. 2008, 2009; Zhdankin et al. 2012). One of the alternatives is that magnetic field rotations through angles $\gtrsim 30°$ are boundaries between flux tubes originating at the Sun, while smaller rotations are produced by local turbulence (e.g., Bruno et al. 2001; Borovsky 2008). However, this interpretation can hardly explain the universal log-normal distribution of magnetic field rotations at various temporal scales (Zhdankin et al. 2012; Chen et al. 2015). The ability of coherent structures in heating of solar-wind plasma was questioned by Borovsky & Denton (2011); but there is currently a growing evidence that plasma heating does occur around coherent structures in plasma turbulence (Osman et al. 2011, 2012; Chasapis et al. 2015, 2018).

In this Letter we present the most extensive data set of proton kinetic-scale CSs collected at 1 au using magnetic field measurements at $1/11$ s resolution. Due to the higher resolution, CSs with thickness from a few to ten times smaller than in the previous studies could be resolved. We reveal distinct scale dependencies of the current density and shear angle, as well as the critical current density that is not exceeded statistically. The results indicate that proton kinetic-scale CSs in the solar wind are indeed produced by turbulence cascade, and advance understanding of turbulence dissipation.

2. Data and Methodology

We use measurements of the Wind spacecraft, located at the L1 Lagrangian point about 200 Earth radii from the Earth (Wilson et al. 2021). We use continuous magnetic field measurements at $1/11$ s resolution provided by the Magnetic Field Instrument (Lepping et al. 1995), and proton densities and flow velocities at 3 s cadence provided by the Wind 3DP instrument (Lin et al. 1995). Note that ion densities coincide within a few tens of percent with electron densities provided at about 9 s cadence by the Solar Wind Experiment instrument (Ogilvie et al. 1995). We consider a period of 124 days, from 2010 October 1 to 2011 February 2, except for the first 16 hr on 2010 December 7 when magnetic field measurements at $1/11$ s resolution were not available.

CSs were selected using the partial variance increment (PVI) method (e.g., Greco et al. 2018). We computed a PVI index, $\mathrm{PVI} = (\sum_\alpha \Delta B_\alpha^2(t, \tau)/\sigma_\alpha^2)^{1/2}$, where $\Delta B_\alpha(t, \tau) = B_\alpha(t + \tau) - B_\alpha(t)$ are magnetic field increments of three magnetic field components ($\alpha = X$, Y, Z) and σ_α are standard deviations of $\Delta B_\alpha(t, \tau)$ computed over 2 hr intervals, that is, over a few outer correlation scales of the solar-wind turbulence (Matthaeus et al. 2005). Coherent structures at various temporal scales correspond to non-Gaussian fluctuations with, for example, $\mathrm{PVI} > 5$. We used only a PVI index computed at $\tau = 1/11$ s to focus on the thinnest resolvable coherent structures. This methodology is essentially equivalent to that of Podesta (2017), who used current density estimates $J \propto |\Delta\boldsymbol{B}(t, \tau)|/\tau$ with $\tau = 1/11$ s to identify the most intense currents in the solar wind. Analysis of synthetic magnetic field signals with spectra typical of the solar wind showed that $J \propto |\Delta\boldsymbol{B}(t, \tau)|/\tau$ with $\tau = 1/11$ s provides reasonable current density estimates (Podesta 2017). Note that the instrument noise does not affect the current density estimates and selection of coherent structures in our study, because the magnetometer noise level at frequencies of 0–10 Hz is less than 0.006 nT (Lepping et al. 1995), which is at least six times smaller than the standard

deviation, $\sigma = (\sum_\alpha \sigma_\alpha^2)^{1/2}$, characterizing magnetic field increments $\Delta\boldsymbol{B}(t, \tau)$ at $\tau = 1/11$ s in our interval.

There are different types of coherent structures among the non-Gaussian fluctuations (e.g., Perrone et al. 2016). To select CSs, each of about $2 \cdot 10^5$ continuous clusters of points with $\mathrm{PVI} > 5$ was considered over intervals of ± 1 s, ± 2 s, ± 3 s, and ± 4 s around its center and unit vector $\boldsymbol{x}'$ along the direction of the magnetic field component with the largest variation was computed for each interval using the maximum variance analysis method (e.g., Sonnerup & Scheible 1998). We visually inspected all profiles of $\boldsymbol{B} \cdot \boldsymbol{x}'$ and selected clusters of points with $\boldsymbol{B} \cdot \boldsymbol{x}'$ reversing the sign within at least one of the intervals. We then manually adjusted the boundaries, that is, the regions to the left and to the right of the $\boldsymbol{B} \cdot \boldsymbol{x}'$ reversal, so that each boundary had a duration of at least half a second and excluded events with substantial relative variations of the magnetic field at the boundaries. We also excluded about 10% of events with bifurcated magnetic field profiles (e.g., Gosling & Szabo 2008), to focus on CSs with relatively smooth magnetic field rotation.

The final data set includes 17,043 CSs,[5] which is the most extensive data set of proton kinetic-scale CSs at 1 au. Since the CSs were selected using only a PVI index with $\tau = 1/11$ s, the distributions of CS parameters presented in the next section are biased toward the thinnest resolvable CSs, but this bias does not affect the key conclusions of this study (Section 4). Each CS will be considered in a local coordinate system $\boldsymbol{xyz}$ most suitable for describing local CS structure (e.g., Knetter et al. 2004; Gosling & Phan 2013; Phan et al. 2020): unit vector $\boldsymbol{z}$ is along the CS normal determined by the cross-product of magnetic fields at the CS boundaries; unit vector $\boldsymbol{x}$ is along $\boldsymbol{x}' - \boldsymbol{z} \cdot (\boldsymbol{x}' \cdot \boldsymbol{z})$; unit vector $\boldsymbol{y}$ completes the right-handed coordinate system, $\boldsymbol{y} = \boldsymbol{z} \times \boldsymbol{x}$. Note that vectors $\boldsymbol{x}$ and $\boldsymbol{y}$ determine the local CS surface, while vector $\boldsymbol{z}$ is directed across the CS surface.

Figure 1 presents a CS observed on 2011 February 1. Panel (a) presents the magnetic field magnitude and three components in the Geocentric Solar Ecliptic coordinate system. The magnetic field rotates across the CS through shear angle $\Delta\theta \approx 60°$, while the magnetic field magnitude remains more or less constant. Note that the shear angle is the angle between the magnetic field vectors at the CS boundaries. We characterize the magnetic field magnitude by $\langle B \rangle$, that is, the mean value of magnetic field magnitudes at the CS boundaries, and $\Delta B_{\max}$, that is, the difference of the maximum and minimum values of the magnetic field magnitude within the CS. For the considered CS we have $\langle B \rangle \approx 10$ nT and $\Delta B_{\max} \approx 1.4$ nT. Panel (b) presents three magnetic field components in the local CS coordinate system $\boldsymbol{xyz}$. The B_x component varies from about 5 to -5 nT across the CS; B_y has similar values at the CS boundaries and a bit larger value around the B_x reversal. The normal component B_z is around zero at the CS boundaries, in accordance with definition of the CS normal, and remains small within the CS. We characterize the CS asymmetry by $\langle B_x \rangle$, that is, the mean of the B_x values at the CS boundaries, and the CS amplitude by the absolute value of their difference, denoted as ΔB_x. The considered CS is rather symmetric with $\langle B_x \rangle \approx -0.04$ nT and $\Delta B_x \approx 10.5$ nT. The CS's central region, highlighted in panel (b), corresponds to $|B_x - \langle B_x \rangle| < 0.2\,\Delta B_x$.

---

[5] The list of the current sheets is publicly available at https://zenodo.org/record/5885741.
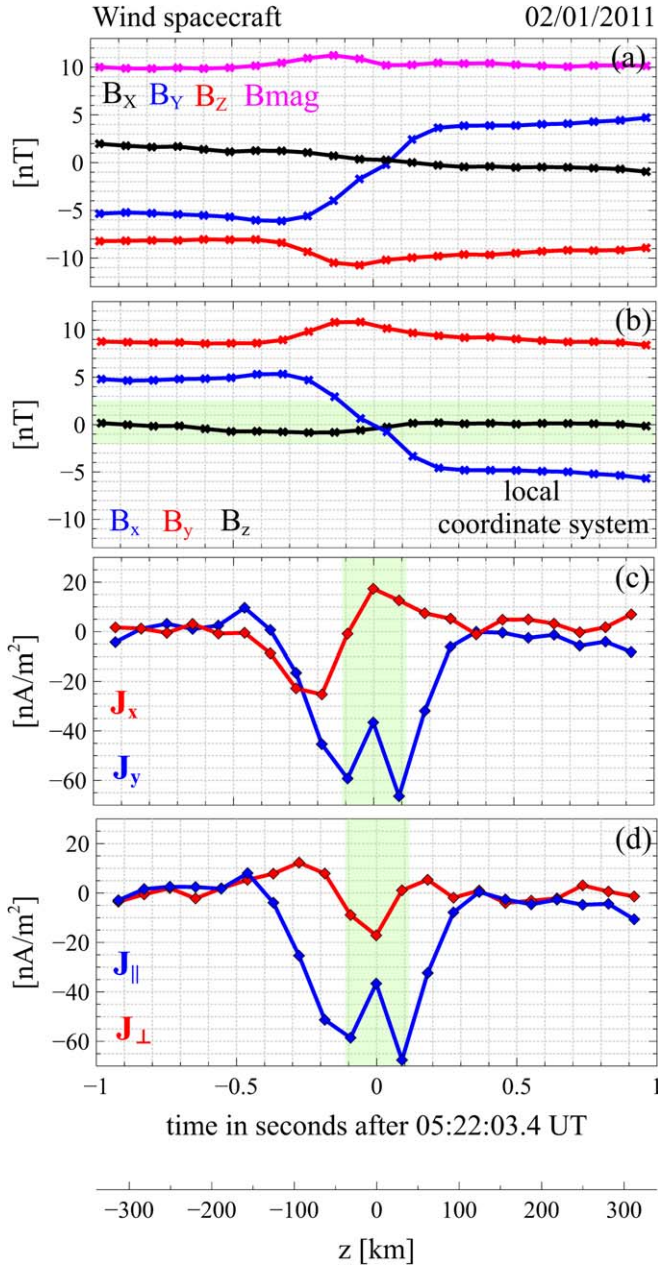
Figure 1. An example of a current sheet observed aboard the Wind spacecraft on 2011 February 1 around 05:22 UT. (a) Magnetic field magnitude and three magnetic field components measured at $1/11$ s resolution (the Geocentric Solar Ecliptic coordinates); (b) three magnetic field components in the local coordinate system **xyz** defined in Section 2; (c) current densities J_x and J_y computed using Equation (1); (d) current densities parallel and perpendicular to the local magnetic field, computed as $J_{||} = (J_xB_x + J_yB_y)/B$ and $J_\perp = (J_yB_x - J_xB_y)/B$. The central region of the CS, $|B_x - \langle B_x \rangle| < 0.2\,\Delta B_x$, is indicated in panels (b)–(d), where $\langle B_x \rangle$ is the mean of the B_x values at the CS boundaries, and ΔB_x is the absolute value of their difference. The bottom horizontal axis presents the spatial coordinate across the CS, $z = -V_n t$, where $t = 0$ corresponds to $B_x = \langle B_x \rangle$ and V_n is the normal component of proton flow velocity measured at the moment closest to the CS.

Panel (c) presents current densities J_x and J_y, estimated as follows:

$$J_y = -\frac{1}{\mu_0 V_n}\frac{dB_x}{dt}, \quad J_x = \frac{1}{\mu_0 V_n}\frac{dB_y}{dt}, \qquad (1)$$

where μ_0 is the vacuum permeability and V_n is the normal component of the proton flow velocity at the moment closest to

the CS. In this estimate we took into account that solar-wind CSs are locally planar structures (e.g., Knetter et al. 2004; Artemyev et al. 2019), so that only the normal component of the proton flow velocity matters, and the Taylor frozen-in hypothesis is valid at spatial scales larger than electron kinetic scales (e.g., Chasapis et al. 2017). The spatial coordinate along the normal, $z = -V_n t$, with $t = 0$ corresponding to $B_x = \langle B_x \rangle$, is shown in Figure 1. We estimate the CS thickness as follows:

$$\lambda = \frac{\Delta B_x}{2\mu_0 \langle J_y \rangle}, \qquad (2)$$

where $\langle J_y \rangle$ is the absolute value of the current density J_y averaged over the CS's central region, $|B_x - \langle B_x \rangle| < 0.2\,\Delta B_x$, highlighted in Figure 1. For the considered CS we have $\lambda \approx 80$ km, or about $1.5\lambda_p$, where λ_p is the proton inertial length. We refer to λ as the CS thickness, but underline that, strictly speaking, λ is a half-thickness, because according to Equation (2) the magnetic field and current density profiles can be approximated as $B_x \approx \langle B_x \rangle + 0.5\Delta B_x \tanh(z/\lambda)$ and $J_y \approx \langle J_y \rangle \operatorname{sech}^2(z/\lambda)$.

Panel (d) presents current densities parallel and perpendicular to the local magnetic field, computed as $J_{||} = (J_xB_x + J_yB_y)/B$ and $J_\perp = (J_yB_x - J_xB_y)/B$. Since the perpendicular current density is statistically much smaller than the parallel current density (Section 4), we quantify the CS intensity by J_0, that is, the absolute value of the parallel current density $J_{||}$ averaged over the CS's central region, and J_{peak}, that is, the absolute peak value of the parallel current density $J_{||}$ within the CS. For the considered CS we have $J_0 \approx 52$ nA m^{-2} and $J_{\text{peak}} \approx 68$ nA m^{-2}. We compare the CS intensities to local Alfvén current density, J_A, defined as the current density corresponding to the drift between protons and electrons of local Alfén speed V_A:

$$J_A = eN_pV_A, \quad V_A = \frac{\langle B \rangle}{(\mu_0 N_p m_p)^{1/2}}, \qquad (3)$$

where e and m_p are proton charge and mass, and N_p is the closest measurement of proton density. For the considered CS, the proton density was around 21 cm^{-3} and we obtain $J_0 \approx 0.3\,J_A$ and $J_{\text{peak}} \approx 0.4\,J_A$. In the next section we present results of the statistical analysis performed using the described methodology.

3. Statistical Results

Figure 2 presents statistical distributions of various CS parameters. Panel (a) shows that the magnetic field magnitude across the CSs is almost constant: $\Delta B_{\max}$ is less than $0.15\langle B \rangle$ for more than 95% of the CSs, that is, in accordance with previous studies of larger-scale CSs (e.g., Burlaga et al. 1977; Vasquez et al. 2007; Artemyev et al. 2019). The CSs are typically asymmetric, that is, the values of B_x at the CS boundaries are different: only about 50% of the CSs satisfy $\langle B_x \rangle \lesssim 0.1\,\Delta B_x$. Panel (b) shows that the current densities J_0 are within 15 nA m^{-2} for more than 95% of the CSs. The most probable value of the current densities J_{peak} is around 5 nA m^{-2}, that is, in accordance with current density estimates in the solar wind by Podesta (2017). Panel (c) shows that the thickness of the CSs is in a range between about 20 and 1000 km, with the most probable value around 100 km. Note that resolving the CSs with thickness of a few tens of kilometers was possible due to a relatively small normal component, V_n, of the proton flow velocity for those CSs.
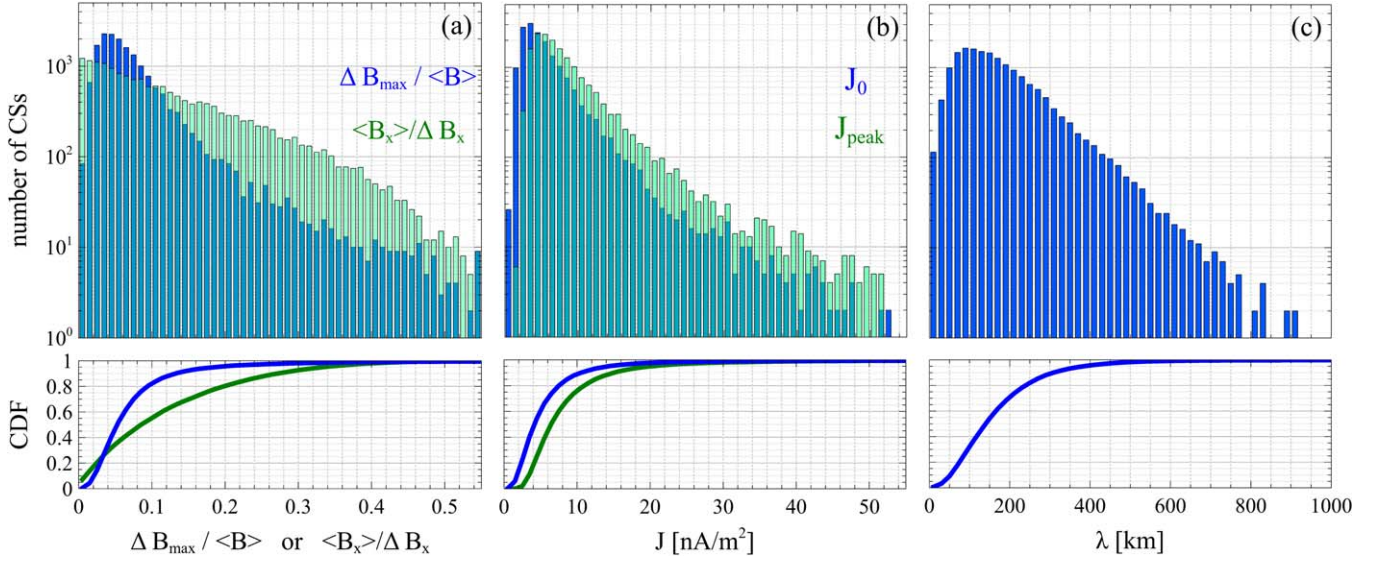
Figure 2. Statistical distributions of various parameters of 17,043 solar wind CSs: (a) $\Delta B_{\max}/\langle B\rangle$, the maximum relative variation of the magnetic field magnitude within the CS, and parameter $\langle B_x\rangle/\Delta B_x$, characterizing the CS asymmetry, where $\langle B_x\rangle$ is the mean of the B_x values at the CS boundaries and ΔB_x is the absolute value of their difference; (b) absolute value J_0 of parallel current density $J_\parallel$ averaged over the CS's central region (see, e.g., Figure 1) and peak value $J_{\rm peak}$ of parallel current density $J_\parallel$ within the CS; (c) CS thickness λ. The bottom panels present cumulative distribution functions of the statistical distributions in the upper panels.
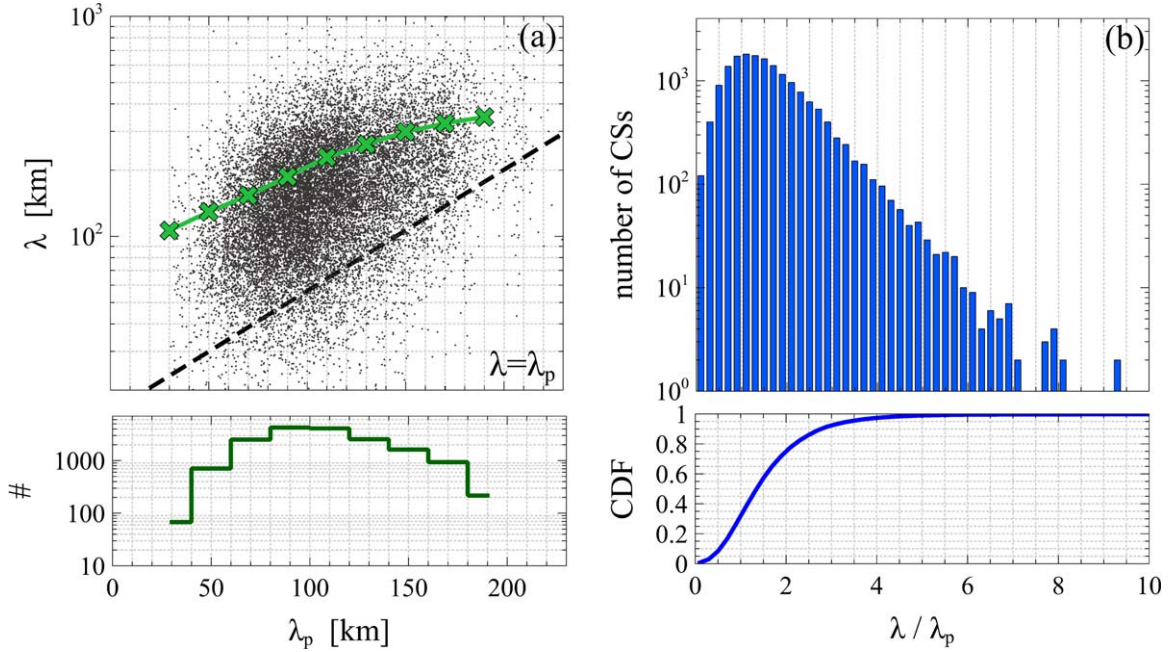

Figure 3. Panel (a) presents a scatter plot of the CS thickness λ vs. local proton inertial length λ_p. The green curve shows the trend that is obtained by sorting the CSs into bins corresponding to various spatial scales and computing the averaged thickness of the CSs within each bin. The number of CSs within each bin is shown in the bottom panel. The black dashed line represents $\lambda = \lambda_p$ for reference. Panel (b) presents a statistical distribution of the CS thickness in units of proton inertial length. The bottom panel presents the corresponding cumulative distribution function.

Figure 3 shows that the CSs are proton kinetic-scale structures with some fraction on sub-proton scales. Panel (a) demonstrates that the CS thickness λ is statistically larger in solar-wind plasma with larger proton inertial length λ_p. A similar trend is observed between the CS thickness and thermal proton gyroradius $\rho_p = \lambda_p \beta_p^{1/2}$, because the proton beta β_p is in a range between 0.4 and 2 for more than 80% of the CSs in our data set as well as in the solar wind in general (e.g., Wilson et al. 2018). Panel (b) presents a statistical distribution of λ/λ_p and shows that the thickness of the CSs is in a range between about 0.1 and $10\lambda_p$, with the most probable value around λ_p. A

similar distribution of λ/ρ_p shows that the most probable value of the CS thickness is around ρ_p. Thus, the typical thickness of the CSs is from a few to ten times smaller than of those in previous statistical studies (e.g., Burlaga et al. 1977; Vasquez et al. 2007; Artemyev et al. 2019). The resolution of these kinetic-scale CSs became possible due to the higher temporal resolution of magnetic field measurements aboard the Wind spacecraft.

Figure 4 presents analysis of the CS current density and its dependence on the CS thickness. Panel (a) shows a scatter plot of J_0 versus λ. We sorted the CSs into bins corresponding to
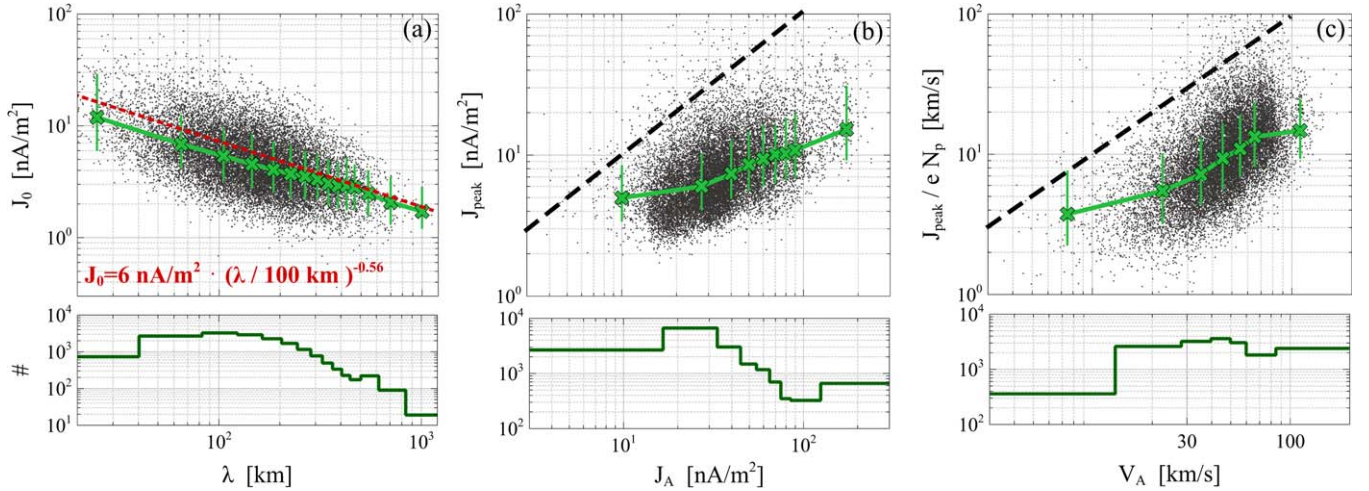
Figure 4. Scatter plots of (a) averaged current density J_0 vs. CS thickness λ; (b) peak current density J_{peak} vs. local Alfvén current density $J_A = eN_pV_A$, where e is the proton charge, N_p is the proton density, V_A is the local Alfvén speed; (c) the peak value of the drift velocity between ions and electrons J_{peak}/eN_p vs. local Alfvén speed V_A. For each of the scatter plots, we sorted the CSs into bins corresponding to different values of the quantities on the x-axis and computed median values of the quantities on the y-axis for the CSs within each bin. The CSs were sorted in such a way that each bin contains a sufficiently large (i.e., more than 100) number of CSs, and the number of CSs within each bin is presented in the bottom panels (only the last bin in panel (a) contains fewer than 100 CSs). The corresponding median profiles are presented by green curves in panels (a)–(c), while error bars correspond to 15th and 85th percentiles of the quantities within each bin. The red line in panel (a) presents the best fit of the scattered data by a power-law function, and the best-fit parameters are indicated in the panel.

different spatial scales and computed the median current density value within each bin. Panel (a) shows the median current density profile along with error bars corresponding to the 15th and 85th percentiles of the current density within each bin. The number of CSs within each bin is shown at the bottom of panel (a). The median profile shows that the CSs with smaller thickness tend to be more intense. Least-squares fitting of all the scattered data by a power-law function reveals the following best fit:

$$J_0 = 6 \text{ nA m}^{-2} \cdot \left(\frac{\lambda}{100 \text{ km}}\right)^{-0.56}, \qquad (4)$$

which is shown in panel (a). Statistical analysis based on the bootstrap method showed that the multiplier (that is, 6 nA m^{-2} factor) is uncertain by less than 20%, while the power-law index is between -0.64 and -0.48 at 98% confidence level. Panel (b) presents a comparison between the peak current densities J_{peak} and local Alfvén current densities J_A. First, the CSs tend to be more intense in solar-wind plasma with larger Alfvén current density. Second, the peak current densities are statistically below local Alfvén current density, $J_{peak} < J_A$, for more than 99% of the CSs, and $J_{peak} < J_A/2$ for 97% of the CSs.

Panel (c) shows there is a positive correlation between local Alfvén speed V_A and J_{peak}/eN_p that is the peak value of the drift velocity between ions and electrons. Thus, the positive correlation between J_{peak} and J_A in panel (b) is not a trivial effect of plasma density variation. The physics behind the correlation of the two seemingly unrelated quantities in panel (c) will be discussed in the next section. Trends and correlations similar to those in panels (b) and (c) are also observed for the averaged current densities J_0. It is noteworthy there is not any correlation between J_{peak}/eN_p or J_0/eN_p and local ion-acoustic speed $(T_e/m_p)^{1/2}$, where T_e is the local electron temperature. The ion-acoustic speed in our data set is in a range from 40 to 60 km/s for more than 95% of the CSs,

while the drift velocities J_{peak}/eN_p vary over almost two orders of magnitude.

Figure 5 reveals remarkable scale dependencies of the normalized intensity, normalized amplitude, and shear angle of the CSs. To demonstrate the scale dependence of a specific quantity, we sorted the CSs into bins corresponding to different spatial scales, and computed the median as well as 15th and 85th percentile values of the quantity within each bin. The number of the CSs within each bin is shown in the bottom panels. Panel (a) presents the scatter plot of J_0/J_A versus λ/λ_p. Similarly to the trend given by Equation (4) in physical units, the median profile shows that the CSs with smaller normalized thickness have larger normalized current densities. Least-squares fitting of all the scattered data by a power-law function reveals the following best fit:

$$J_0/J_A = 0.17 \cdot (\lambda/\lambda_p)^{-0.51}, \qquad (5)$$

which is shown in panel (a) and rather well describes the median profile. Analysis based on the bootstrap method showed that the multiplier is uncertain by about 10%, while the power-law index is between -0.6 and -0.4 at 98% confidence level. Panel (b) presents the scatter plot of $\Delta B_x/\langle B \rangle$ versus λ/λ_p. The median profile reveals a clear scale dependence: the CSs with larger normalized thickness have larger normalized amplitudes. Least-squares fitting of all the scattered data by a power-law function reveals the following best fit:

$$\Delta B_x/\langle B \rangle = 0.33 \cdot (\lambda/\lambda_p)^{0.49}, \qquad (6)$$

which again well describes the median profile. Note that this scaling relation could be foreseen based on Equation (5), because $J_0 \approx \Delta B_x/2\mu_0\lambda$ and $J_A = eN_pV_A = \langle B \rangle/\mu_0\lambda_p$. The multiplier in Equation (6) is uncertain by about 10%, while the power-law index is between 0.4 and 0.6 at 98% confidence level. Since in a CS with more or less constant magnetic field magnitude, $\Delta B_x/\langle B \rangle$ is unambiguously related to the shear angle, we expect to observe a positive correlation and similar trend between $\Delta\theta$ and λ/λ_p. Panel (c) confirms the scale dependence of the shear angle with
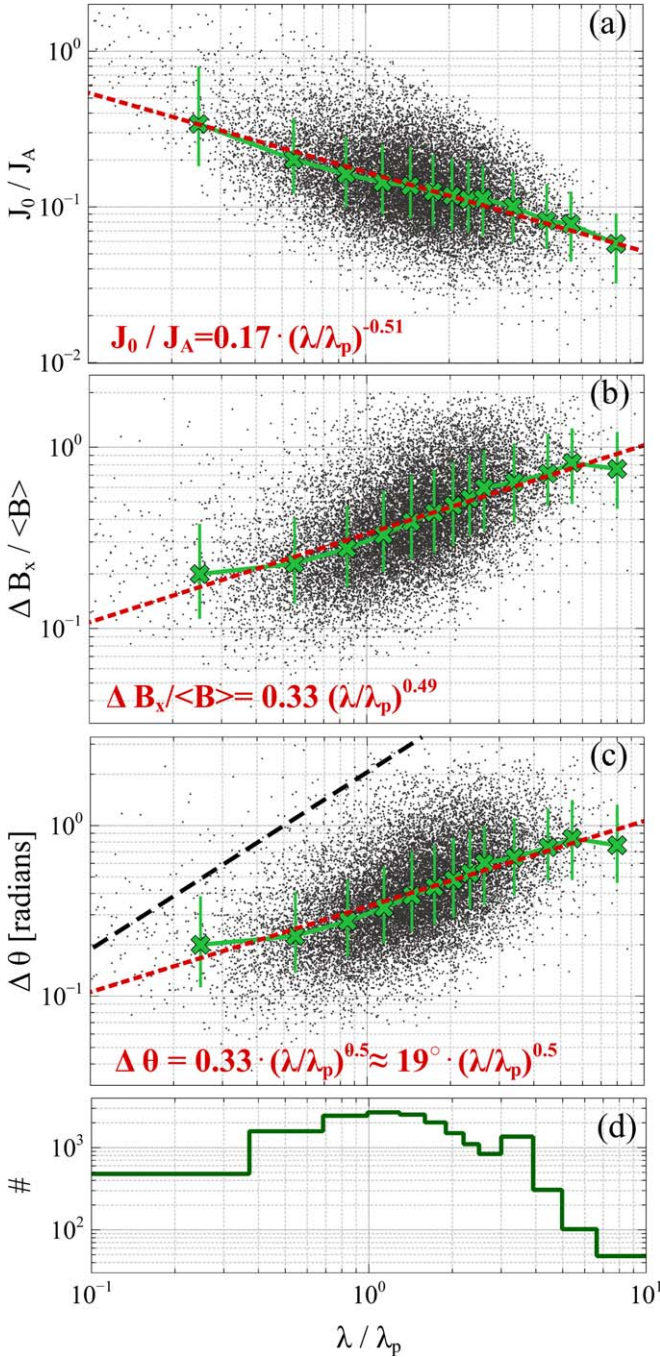
Figure 5. Scatter plots of (a) the current density normalized to Alfvén current density J_0/J_A vs. normalized CS thickness λ/λ_p; (b) the CS amplitude normalized to the mean magnetic field magnitude $\Delta B_x/\langle B\rangle$ vs. λ/λ_p; (c) magnetic shear angle $\Delta\theta$ vs. λ/λ_p. The CSs were sorted into bins corresponding to different values of normalized CS thickness, and median values of the quantities in panels (a)–(c) were computed within each bin. The CSs were sorted in such a way that each bin contains a sufficiently large (i.e., more than 100) number of CSs within each bin, and the number of CSs within each bin is presented in panel (d) (only the last bin contains fewer than 100 CSs). Panels (a)–(c) present the median profiles (green curves) along with error bars corresponding to 15th and 85th percentiles within each bin. The panels also indicate the best power-law fits of the scattered data (red curves) along with the best-fit parameters. The dashed line in panel (c) corresponds to $\Delta\theta = 2\lambda/\lambda_p$, which corresponds to $J_\parallel = J_A$.

the following best fit of the scattered data:

$$\Delta\theta = 0.33 \cdot (\lambda/\lambda_p)^{0.5} \approx 19° \cdot (\lambda/\lambda_p)^{0.5}, \qquad (7)$$

which well describes the median profile. The uncertainties of the best-fit parameters are identical to those of the best-fit parameters in Equation (6). There is a scale-dependent upper threshold on the shear angles, $\Delta\theta \lesssim 2\,\lambda/\lambda_p$, for more than 99% of the CSs and $\Delta\theta \lesssim \lambda/\lambda_p$ for about 97% of the CSs.

4. Theoretical Interpretation and Discussion

We presented the analysis of proton kinetic-scale CSs in the solar wind based on the most extensive data set collected at 1 au. Certainly, this data set does not include all CSs present in the considered interval. We selected the CSs using a PVI index with a minimum time increment $\tau = 1/11$ s and, therefore, our data set and statistical distributions in Figures 2 and 3 are biased toward the thinnest resolvable CSs. The use of PVI indexes at larger increments would be essentially equivalent to the use of magnetic field measurements at a lower resolution. Therefore, the previous studies based on a lower-resolution magnetic field may demonstrate the results of using larger increments in our procedure. The studies based on magnetic field measurements at a few second resolution resolved CSs with typical thickness around 1000 km (Burlaga et al. 1977; Lepping & Behannon 1986; Söding et al. 2001; Artemyev et al. 2019), while the use of magnetic field measurements at 1/3 s resolution allowed resolving CSs with typical thickness around a few hundred kilometers; these CSs turned out to be one order of magnitude more abundant than CSs resolved at a few second resolution (Vasquez et al. 2007). We used magnetic field measurements at 1/11 s resolution and resolved CSs with typical thickness around 100 km and averaged occurrence rate $(17{,}043/124 \approx 140\ \text{CSs/day})$ comparable with that reported by Vasquez et al. (2007). Thus, the higher resolution of the magnetic field measurements allowed us to collect truly kinetic-scale CSs, which are thinner than those reported in previous studies. Although our data set does not include CSs of all possible spatial scales, the collection of which would require repeating our selection procedure with different increments of τ, this data set allows us to address the structure and origin of kinetic-scale CSs in the solar wind.

4.1. Local Structure of Solar Wind Current Sheets

Since solar wind CSs are locally planar structures (e.g., Knetter et al. 2004; Artemyev et al. 2019), we can describe the local magnetic field of the CSs as follows:

$$\boldsymbol{B} = B(z)\sin\theta(z)\,\boldsymbol{x} + B(z)\cos\theta(z)\,\boldsymbol{y} + B_z\,\boldsymbol{z}, \qquad (8)$$

where $\theta(z)$ and $B(z)$ determine, respectively, the magnetic field rotation and magnetic variation within a CS; the normal component B_z is much smaller than $B(z)$. The shear angle $\Delta\theta$ estimated in our experimental analysis corresponds to the difference of θ values at the CS boundaries. Note that Equation (8) provides the most general description of a CS with nonzero B_y. The specific models, such as a Harris CS with a constant B_y or a force-free Harris CS, often used in reconnection simulations and theoretical studies (e.g., Landi et al. 2015) are special cases of Equation (8) corresponding to particular profiles of $B(z)$ and $\theta(z)$.

Simple calculations show that current densities parallel and perpendicular to the local magnetic field, $J_\parallel = (J_x B_x + J_y B_y)/B$ and $J_\perp = (J_y B_x - J_x B_y)/B$, determine, respectively, the

magnetic field rotation and magnitude variation within a CS:

$$J_{\parallel} = \frac{B}{\mu_0}\frac{d\theta}{dz}, \qquad J_{\perp} = \frac{1}{\mu_0}\frac{dB}{dz}. \qquad (9)$$

The amplitudes of the parallel and perpendicular current densities can then be estimated as $J_{\parallel} \approx (c/4\pi)\langle B\rangle\Delta\theta/2\lambda$ and $J_{\perp} \approx (c/4\pi)\Delta B_{\mathrm{max}}/2\lambda$. First, these estimates show that the current-density limitation $J_{\parallel} \lesssim J_A$ (Figure 4(b)) is equivalent to the scale-dependent upper threshold on shear angles, $\Delta\theta \lesssim 2\lambda/\lambda_p$ (Figure 5(c)). Second, they show that the relatively small variations of the magnetic field magnitude within the CSs (Figure 2(a)) imply that the current density is dominated by the parallel component. The ratio $J_{\perp}/J_{\parallel} \approx \Delta B_{\mathrm{max}}/\langle B\rangle\Delta\theta$ is less than 0.3 for more than 95% of the CSs (not shown). The small variations of the magnetic field magnitude also imply that the plasma pressure variation across the CSs is much smaller than the magnetic field pressure. The pressure balance $p + B^2/8\pi = \mathrm{const}$ shows that the maximum variation of the plasma pressure across the CSs is $\Delta p_{\mathrm{max}} \approx \langle B\rangle\Delta B_{\mathrm{max}}/4\pi$, while its ratio to the typical magnetic field pressure is $\Delta p/p_B \approx 2\Delta B_{\mathrm{max}}/\langle B\rangle$. According to Figure 2(a), this ratio does not exceed 0.3 for more than 95% of the CSs. The dominance of the parallel current density and relatively small variations of the plasma pressure show that the kinetic-scale CSs in the solar wind are statistically more or less force-free.

4.2. Current Sheets and Turbulence

The turbulence in the solar wind is dominated by magnetic field fluctuations highly oblique to the mean magnetic field, with a power-law spectrum $E_{k_{\perp}} \propto k_{\perp}^{-\nu}$, where $\nu \approx 5/3$ in the inertial range, $k_{\perp}\lambda_p \lesssim 1$, and $\nu \approx 2.8$ at $k_{\perp}\lambda_p \gtrsim 1$ (see, e.g., review by Chen 2016). The rms amplitude, δb_{λ} of turbulent fluctuations at spatial scale λ can be then estimated as $\delta b_{\lambda} \propto (E_{k_{\perp}}\Delta k_{\perp})^{1/2} \propto \lambda^{(\nu-1)/2}$, where we take into account that $\Delta k_{\perp} \propto k_{\perp} \propto \lambda^{-1}$. The corresponding current density is $j_{\lambda} \propto \delta b_{\lambda}/\lambda \propto \lambda^{(\nu-3)/2}$. In the inertial range, $k_{\perp}\lambda_p \lesssim 1$, we expect

$$\delta b_{\lambda} \propto \lambda^{1/3}, \quad j_{\lambda} \propto \lambda^{-2/3}, \qquad (10)$$

while at $k_{\perp}\lambda_p \gtrsim 1$ we expect

$$\delta b_{\lambda} \propto \lambda^{0.9}, \quad j_{\lambda} \propto \lambda^{-0.1}. \qquad (11)$$

Thus, the rms amplitudes of the turbulent magnetic field and current density fluctuations should be scale dependent (e.g., Schekochihin et al. 2009; Boldyrev & Perez 2012). Since the magnetic shear angle, $\delta\theta_{\lambda}$, is proportional to δb_{λ}, it should be similarly scale-dependent.

We have found that amplitudes, current densities, and shear angles of proton kinetic-scale CSs are scale dependent in a fashion similar to that of turbulent fluctuations. Moreover, the CS amplitude scales with the CS thickness as $\Delta B_x/\langle B\rangle \propto (\lambda/\lambda)^{0.49}$, so that the power-law index is between $1/3$ and 0.9, which are expected for turbulent fluctuations at scales above and below proton kinetic scales. Similarly, the CS intensity scales with the CS thickness as $J_0/J_A \propto (\lambda/\lambda_p)^{-0.51}$ with the power-law index between $-2/3$ and -0.1. These scale dependencies are strong indications that proton kinetic-scale CSs are produced locally by plasma turbulence. This

conclusion is not affected by the uncertainties of the power-law indexes characterizing the scale-dependent properties of the CSs (Section 3).

The critical question is whether the scale dependencies revealed in Figure 5 would be affected if we included all kinetic-scale CSs present in the considered interval, rather than used the data set biased toward the thinnest resolvable CSs. The strong indication that the revealed scale dependencies would not be affected is that they are consistent with the scale-dependent properties of magnetic field rotations in the solar wind (Zhdankin et al. 2012; Chen et al. 2015). These studies showed that statistical distributions of angles $\alpha(\tau)$ between magnetic fields $\boldsymbol{B}(t)$ and $\boldsymbol{B}(t+\tau)$ in the solar wind behave similarly at various temporal scales. More precisely, $\alpha(\tau)$ normalized to its mean value $\langle\alpha\rangle$ is described by a universal log-normal distribution independent of τ. In turn, the mean value scales with τ as $\langle\alpha\rangle \propto \tau^{0.46}$, so that magnetic field rotation angles are larger at larger spatial scales (see also Perri et al. 2012). This is qualitatively, and even quantitatively, consistent with the scale dependence of magnetic shear angles across the CSs, $\Delta\theta \propto (\lambda/\lambda_p)^{0.5}$, revealed in our analysis. Thus, we believe that inclusion of kinetic-scale CSs, which could be selected using PVI indexes at larger increments, would not affect our conclusion that kinetic-scale CSs are produced by turbulence cascade.

4.3. Current Density Limitation Mechanisms

We have found that the peak value of the current density within a CS is correlated with local Alfvén current density J_A, while the drift velocity between ions and electrons is correlated with local Alfvén speed V_A. In principle, a positive correlation between these quantities should be expected, because J_A and V_A are natural units of the current density and velocities in MHD and Hall-MHD turbulence simulations (e.g., Papini et al. 2019). The intriguing property, though, is that the peak value J_{peak} of the current density does not statistically exceed J_A and, actually, even $J_A/2$. There are several scenarios capable of explaining the observed current-density limitation. The first scenario is that once the parallel current density exceeds the local Alfvén current some instability may lead to a current-density limitation or a CS destruction. One of the known instabilities is the so-called Alfén instability that was considered by Voitenko (1995) and Bellan (1999) for a force-free CS at low plasma betas. The relevance of this instability to solar wind CSs at realistic plasma betas requires a separate analysis. The ion-acoustic instability is highly unlikely to be relevant to current density limitation, because we have found no correlation between the ion-electron drift velocity J_{peak}/eN_p and the local ion-acoustic speed (see also Boldyrev et al. 2015). The second scenario is that once the ion-electron drift velocity becomes comparable with the local Alfvén speed, more electrons can be in the Landau resonance with ambient turbulence (e.g., TenBarge & Howes 2013), which potentially results in electron scattering and current density limitation.

4.4. Our Data Set and Assumptions of the Single-spacecraft Analysis

The Wind spacecraft allowed us to select the most extensive data set of proton kinetic-scale CSs in the solar wind not disturbed by the Earth's bow shock. In our single-spacecraft analysis CS normals were determined by the cross-product of

magnetic fields at the CS boundaries, which works relatively well according to the multispacecraft study by Knetter et al. (2004). Multispacecraft studies would certainly allow more accurate estimates of CS normals, but the available multi-spacecraft missions often probe the solar wind disturbed by the Earth's bow shock and require careful data selection.

We repeated the analysis presented in this Letter for the current densities and thickness estimated via Equations (1) and (2) but using proton flow velocity magnitude in the *yz* plane rather than along CS normals *z*. The so-obtained quantities represent lower estimates of the current densities and upper estimates of the CS thickness, which are independent of the exact knowledge of CS normals. We found similar scale dependencies with only slightly different fitting parameters: $J_0 \approx 6 \text{ nA m}^{-2} \cdot (\lambda/100 \text{ km})^{-0.49}$, $J_0/J_A \approx 0.14 \cdot (\lambda/\lambda_p)^{-0.4}$, $\Delta B_x/\langle B \rangle \approx 0.28 \cdot (\lambda/\lambda_p)^{0.6}$, and $\Delta\theta \approx 15° \cdot (\lambda/\lambda_p)^{0.62}$. Thus, we feel confident that the results of our single-spacecraft analysis reflect realistic properties of proton kinetic-scale CSs in the solar wind.

5. Conclusions

The results of this Letter can be summarized as follows:

1. The proton kinetic-scale CSs in the solar wind are statistically force-free and typically asymmetric.
2. The current density within the CSs is scale-dependent, with CSs of smaller thickness being more intense. The magnetic field amplitude and magnetic shear angle are scale-dependent, as well.
3. The drift velocity between electrons and ions in the CSs tends to be larger in the solar wind with larger Alfvén speed. The current density does not statistically exceed local Alfvén current density.

Based on these observations, we argue that proton kinetic-scale CSs in the solar wind are produced locally by turbulence, and some mechanism, either CS instability or scattering of electrons by ambient turbulence, should keep the current density below the local Alfvén current density.

ORCID iDs

I. Y. Vasko https://orcid.org/0000-0002-4974-4786
T. Phan https://orcid.org/0000-0002-6924-9408
S. D. Bale https://orcid.org/0000-0002-1989-3596
F. S. Mozer https://orcid.org/0000-0002-2011-8140

References

Artemyev, A. V., Angelopoulos, V., Halekas, J. S., et al. 2018, ApJ, 859, 95
Artemyev, A. V., Angelopoulos, V., & Vasko, I. Y. 2019, JGRA, 124, 3858
Bellan, P. M. 1999, PhRvL, 83, 4768
Boldyrev, S., Chen, C. H. K., Xia, Q., & Zhdankin, V. 2015, ApJ, 806, 238
Boldyrev, S., & Perez, J. C. 2012, ApJL, 758, L44
Borovsky, J. E. 2008, JGRA, 113, A08110
Borovsky, J. E., & Denton, M. H. 2011, ApJL, 739, L61
Bruno, R., Carbone, V., Veltri, P., Pietropaolo, E., & Bavassano, B. 2001, P&SS, 49, 1201
Burlaga, L. F., Lemaire, J. F., & Turner, J. M. 1977, JGR, 82, 3191
Cerri, S. S., & Califano, F. 2017, NJPh, 19, 025007
Cerri, S. S., Servidio, S., & Califano, F. 2017, ApJL, 846, L18
Chasapis, A., Matthaeus, W. H., Parashar, T. N., et al. 2017, ApJL, 844, L9
Chasapis, A., Matthaeus, W. H., Parashar, T. N., et al. 2018, ApJL, 856, L19
Chasapis, A., Retinò, A., Sahraoui, F., et al. 2015, ApJL, 804, L1
Chen, C. H. K. 2016, JPlPh, 82, 535820602
Chen, C. H. K., Matteini, L., Burgess, D., & Horbury, T. S. 2015, MNRAS, 453, L64
Cranmer, S. R., Matthaeus, W. H., Breech, B. A., & Kasper, J. C. 2009, ApJ, 702, 1604
Franci, L., Cerri, S. S., Califano, F., et al. 2017, ApJL, 850, L16
Franci, L., Landi, S., Verdini, A., Matteini, L., & Hellinger, P. 2018, ApJ, 853, 26
Gosling, J. T., & Phan, T. D. 2013, ApJL, 763, L39
Gosling, J. T., & Szabo, A. 2008, JGRA, 113, A10103
Greco, A., Chuychai, P., Matthaeus, W. H., Servidio, S., & Dmitruk, P. 2008, GeoRL, 35, L19111
Greco, A., Matthaeus, W. H., Perri, S., et al. 2018, SSRv, 214, 1
Greco, A., Matthaeus, W. H., Servidio, S., Chuychai, P., & Dmitruk, P. 2009, ApJL, 691, L111
Hellinger, P., TráVníček, P. M., Štverák, Š., Matteini, L., & Velli, M. 2013, JGRA, 118, 1351
Horbury, T. S., Burgess, D., Fränz, M., & Owen, C. J. 2001, GeoRL, 28, 677
Karimabadi, H., Roytershteyn, V., Wan, M., et al. 2013, PhPl, 20, 012303
Knetter, T., Neubauer, F. M., Horbury, T., & Balogh, A. 2004, JGRA, 109, A06102
Kohl, J. L., Strachan, L., & Gardner, L. D. 1996, ApJL, 465, L141
Landi, S., Del Zanna, L., Papini, E., Pucci, F., & Velli, M. 2015, ApJ, 806, 131
Lepping, R. P., Acúna, M. H., Burlaga, L. F., et al. 1995, SSRv, 71, 207
Lepping, R. P., & Behannon, K. W. 1986, JGR, 91, 8725
Lin, R. P., Anderson, K. A., Ashford, S., et al. 1995, SSRv, 71, 125
Matteini, L., Franci, L., Alexandrova, O., et al. 2020, FrASS, 7, 83
Matthaeus, W. H., Dasso, S., Weygand, J. M., et al. 2005, PhRvL, 95, 231101
Matthaeus, W. H., & Lamkin, S. L. 1986, PhFl, 29, 2513
Matthaeus, W. H., & Velli, M. 2011, SSRv, 160, 145
Matthaeus, W. H., Wan, M., Servidio, S., et al. 2015, RSPTA, 373, 20140154
Ogilvie, K. W., Chornay, D. J., Fritzenreiter, R. J., et al. 1995, SSRv, 71, 55
Osman, K. T., Matthaeus, W. H., Greco, A., & Servidio, S. 2011, ApJL, 727, L11
Osman, K. T., Matthaeus, W. H., Wan, M., & Rappazzo, A. F. 2012, PhRvL, 108, 261102
Papini, E., Franci, L., Landi, S., et al. 2019, ApJ, 870, 52
Perri, S., Goldstein, M. L., Dorelli, J. C., & Sahraoui, F. 2012, PhRvL, 109, 191101
Perrone, D., Alexandrova, O., Mangeney, A., et al. 2016, ApJ, 826, 196
Phan, T. D., Bale, S. D., Eastwood, J. P., et al. 2020, ApJS, 246, 34
Podesta, J. J. 2017, JGRA, 122, 2795
Sonnerup, B. U. Ö., & Scheible, M. 1998, ISSIR, 1, 185
Schekochihin, A. A., Cowley, S. C., Dorland, W., et al. 2009, ApJS, 182, 310
Servidio, S., Valentini, F., Perrone, D., et al. 2015, JPlPh, 81, 325810107
Söding, A., Neubauer, F. M., Tsurutani, B. T., Ness, N. F., & Lepping, R. P. 2001, AnGeo, 19, 681
TenBarge, J. M., & Howes, G. G. 2013, ApJL, 771, L27
Tsurutani, B. T., & Smith, E. J. 1979, JGR, 84, 2773
Vasquez, B. J., Abramenko, V. I., Haggerty, D. K., & Smith, C. W. 2007, JGRA, 112, A11102
Voitenko, Y. M. 1995, SoPh, 161, 197
Wan, M., Matthaeus, W. H., Roytershteyn, V., et al. 2016, PhPl, 23, 042307
Wan, M., Rappazzo, A. F., Matthaeus, W. H., Servidio, S., & Oughton, S. 2014, ApJ, 797, 63
Wilson, L. B. I., Brosius, A. L., Gopalswamy, N., et al. 2021, RvGeo, 59, e2020RG000714
Wilson, L. B., III, Stevens, M. L., Kasper, J. C., et al. 2018, ApJS, 236, 41
Zhdankin, V., Boldyrev, S., & Mason, J. 2012, ApJL, 760, L22
Zhdankin, V., Boldyrev, S., Perez, J. C., & Tobias, S. M. 2014, ApJ, 795, 127
Zhdankin, V., Uzdensky, D. A., Perez, J. C., & Boldyrev, S. 2013, ApJ, 771, 124